Flow (2025), **5** E33
doi:10.1017/flo.2025.10027

FLOW CAMBRIDGE UNIVERSITY PRESS

RESEARCH ARTICLE

Wall shear stress generated by a Bernoulli pad: experiments and numerical simulations

Anshul S. Tomar[1], Shaede Perzanowski[1], Ricardo Mejia-Alvarez[1], Ranjan Mukherjee[1], Aren Hellum[2] and Kristina Kamensky[2]

[1]Michigan State University, East Lansing, MI, USA
[2]Naval Undersea Warfare Center, Newport, RI, USA
Corresponding author: Ranjan Mukherjee; Email: mukherji@egr.msu.edu

Received: 17 March 2025; **Revised:** 24 July 2025; **Accepted:** 26 August 2025

Keywords: Bernoulli pad; biofouling mitigation; CFD; flow separation; hot-film anemometer; non-contact cleaning; shear-based cleaning; wall shear measurements

Abstract

Bernoulli pads generate locally large wall shear stresses on workpieces, which can be used for cleaning, but may also damage delicate surfaces. This work presents direct measurements of the wall shear stress using constant-temperature anemometry for the first time. A hot-film sensor was calibrated in the laminar and turbulent flow regimes using a purpose-built water flow channel. The calibrated sensor was then flush mounted onto a smooth surface and a Bernoulli pad was traversed over the sensor and wall shear stress data were acquired. Numerical simulations of the flow field were also performed; they accurately predicted the maximum shear stress near the jet corner but over-predicted at large radii.

Impact Statement

Biological organisms accumulate on the hulls of ships, leading to increased energy consumption, higher maintenance costs and the transport of invasive organisms. Fouling-release coatings which allow organisms to be removed by shear are prone to mechanical damage and are not effective when the ship is stationary. A Bernoulli pad confines a high-speed jet of fluid to a small gap, producing a normal force which maintains the gap and wall shear which can be used to clean the hull. This flow field is separated near the jet core, transitioning and highly confined, which makes it difficult to study experimentally and challenging to model. In particular, the shear force produced by a pad as a function of radial position has not been measured. In this work, we measure the wall shear stress of a Bernoulli pad using hot-film anemometry. We also compare these results with numerical simulations, and discuss shortcomings observed in the modelling results.

1. Introduction

A Bernoulli pad is conventionally used to pick and place objects without contacting them (Paivanas & Hassan 1981); Misimi *et al.* 2016). The pad is proximally located to an object or a workpiece, and axial flow through the centre of the pad impinges on the workpiece and is deflected radially outward. The centre of this impingement region is a stagnation point, where pressure is the highest – see figure 1. As the flow is deflected radially outward in the impingement region, the gauge pressure decreases gradually but

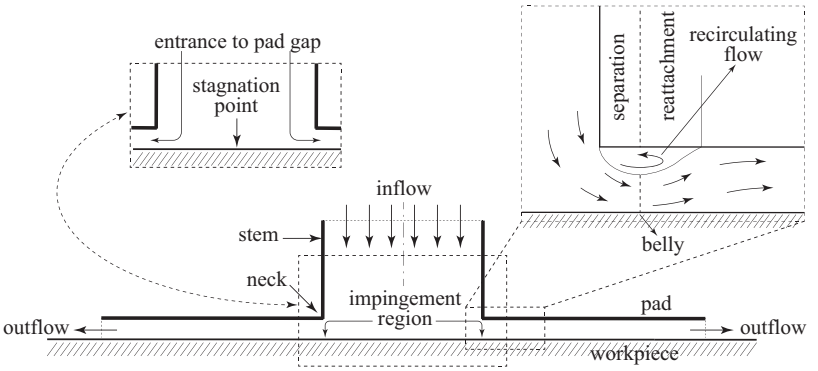

Figure 1. *A Bernoulli pad, located proximally to a workpiece, showing inflow, outflow, impingement region, stagnation point and recirculation region.*

remains positive as it approaches the entrance to the pad's gap. As such, the pressure in this impingement region tends to repel the workpiece. The drastic increase in velocity due to the cross-section reduction at the entrance to the pad's gap induces a pressure drop down to vacuum levels. As the flow expands radially outward inside the pad's gap, the intensity of this vacuum reduces gradually. The vacuum present in the pad's gap induces an attractive force on the workpiece. The balance between the repulsive force from the impingement region and the attractive force from the pad's gap tends to fix the gap at a constant value. Any effort to take the pad from this equilibrium configuration is met with a resistive force. The effect of the gap on the nature of the normal force (attractive or repulsive) has been widely discussed in the literature (Li & Kagawa 2014). The change in the nature of the force gives rise to both stable and unstable equilibrium configurations (Tomar *et al.* 2022) but the presence of the stable equilibrium configuration allows the Bernoulli pad to be used for pick and place operations in industry (McIlwraith & Christie 2003); Wagner *et al.* 2008; Brun & Melkote 2009).

In addition to normal forces, shear forces are generated by the flow field between the pad and the workpiece (Kamensky *et al.* 2019). Flow-induced shear forces generated by a Bernoulli pad have found the application of non-contact biofouling mitigation of ship hulls (Kamensky *et al.* 2020). A Bernoulli-pad device can be used to remove biofouling while the ship is at port, in both wet and dry docking conditions, and can leverage the benefits of fouling-release coatings (Hu *et al.* 2020). The organisms which make up the biofouling colonies can also be altered by repeated application of fluid shear stress (Hunsucker *et al.* 2016). The abrupt change in the direction of flow in a Bernoulli pad introduces separation and recirculation near the neck of the pad (Shi & Li, 2016). The separation and constriction of the flow, shown in figure 1, results in large magnitude shear stresses on the workpiece, which are essential for the application of bio-fouling mitigation.

In our previous work (Tomar *et al.* 2022), we have used computational fluid dynamics simulations to develop a better understanding of the flow physics associated with a Bernoulli pad, including the location and magnitude of the maximum shear stress. It was found that the magnitude of wall shear stress is maximum at the belly of the recirculation region – see figure 1. Resolving the region of flow separation is computationally expensive, which makes it challenging to predict the wall shear stress accurately. The numerical results need validation, and for the first time, in this paper a constant-temperature hot-film anemometer is used with water as the working fluid to measure the wall shear stress. Measurement of the shear stress profile will aid in the design of Bernoulli pads as hull grooming devices and help create cleaning schedules as cleaning efficacy is dependent on the organism and time between grooming (Menesses *et al.* 2017).

Over the last few decades, various methods for wall shear stress measurements have been developed and reviewed in the literature (Winter, 1979; Fernholz *et al.* 1996; Sheplak *et al.* 2006; Naughton and Sheplak, 2002). A method that combines good spatial resolution with the ability to work in water and be

https://doi.org/10.1017/flo.2025.10027 Published online by Cambridge University Press

implemented in a confined geometry with poor optical access is hot-film anemometry. Hot-film sensors have been used to detect flow separation and detection of transition from laminar to turbulent flow – see (Bellhouse & Schultz, 1966; Owen, 1970; Jiang *et al.* 2000), for example. In the present work, we use a flush-mounted hot-film sensor for measurement of wall shear stress generated by a Bernoulli pad. The main principle behind this technique is to correlate heat transfer from the sensor with wall shear stress. To this end, the sensor needs to be calibrated under known wall shear conditions. Under a Bernoulli pad, the maximum wall shear occurs in a very narrow region close to the neck of the pad, but decays rapidly at larger radii (Tomar *et al.* 2022, 2024). This large variation makes it challenging to investigate the wall shear stress experimentally.

Experimental investigations with Bernoulli pads have been reported in the literature. Li and Kagawa (2014), Li *et al.* (2024), Yu *et al.* (2022) and Mykhailyshyn *et al.* (2022), for example, conducted experiments to understand the various factors that affect the wall-normal forces. A majority of the investigations in the literature have focused on wall-normal forces and used air as the working fluid. To the best of our knowledge, the only works using water as the working fluid were reported by Li *et al.* (2024) and Kamensky (2020). The work by Li *et al.* (2024) focused on the normal force and pressure distribution generated by the flow field, whereas particle tracking velocimetry (PTV) experiments were conducted to measure the velocity components of the flow field in Kamensky (2020). It is difficult to get accurate velocity measurements and thereby shear stresses near the wall using particle velocimetry methods without significant magnification – see Kahler *et al.* (2012). The geometry of the Bernoulli pad makes this particularly challenging. Hence, the wall shear measurements presented in this work fill an important gap in the literature. It should be mentioned that experimental studies on radial suction flow and its effect on a water vortex unit were carried out in Lyu *et al.* (2024). Although water is used as the working fluid, the work focused on normal suction forces and not shear force measurements.

This paper is organised as follows. A brief review of channel flow and the working principle of hot-film sensors is provided in Section 2. The hot-film sensor is calibrated using fully developed channel flow; an analytical solution for wall shear in channel flow is presented in Section 2 and the procedure for calibration of the hot-film sensor is presented in Section 3. The experimental set-up for wall shear measurements is described in Section 4. Section 5 provides experimental results and compares them with results obtained from numerical simulations. Concluding remarks are provided in Section 6.

2. Background

2.1. Analytical solution for wall shear in channel flow

For two-dimensional steady-state fully developed channel flow – see figure 2, the Navier–Stokes equation for the streamwise velocity becomes

$$\mu \frac{\mathrm{d}^2 u}{\mathrm{d}y^2} = \frac{\mathrm{d}p}{\mathrm{d}x},$$

where $p = p(x)$ is the pressure, $u = u(y)$ is the streamwise velocity and μ denotes the dynamic viscosity. On integrating the above equation with respect to y once, and substituting the symmetry condition $du/dy = 0$ at $y = h/2$, we get

$$\mu \frac{\mathrm{d}u}{\mathrm{d}y} = \left(y - \frac{h}{2}\right) \frac{\mathrm{d}p}{\mathrm{d}x}. \tag{2.1}$$

Note that h is the channel's height. This result does not assume any particular flow regime, laminar or turbulent. From the above result, the shear stress τ can be written as

$$\tau \triangleq \mu \frac{\mathrm{d}u}{\mathrm{d}y} = \left(y - \frac{h}{2}\right) \frac{\mathrm{d}p}{\mathrm{d}x}.$$

https://doi.org/10.1017/flo.2025.10027 Published online by Cambridge University Press

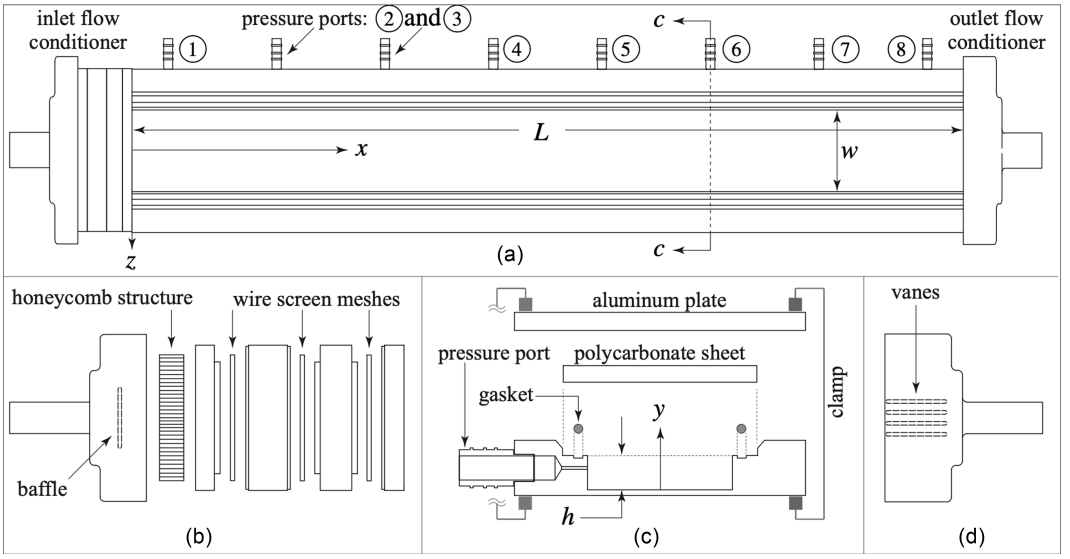

Figure 2. *Channel set-up used for calibration of the hot-film sensor; figures are not drawn to scale: (a) top view of the channel showing the eight pressure ports, (b) exploded view of the inlet flow conditioner, (c) exploded view of section c–c of channel with gasket, polycarbonate sheet, aluminium plate and clamps and (d) outlet flow conditioner showing internal vanes.*

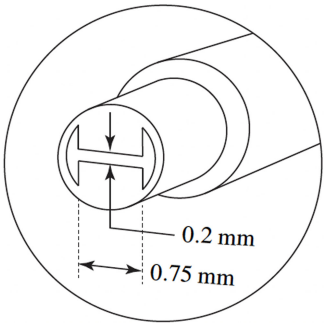

Figure 3. *A schematic of the hot-film sensor 55R46 by Dantec dynamics (Dantec, 2023).*

At the wall, where $y = 0$, the wall shear stress τ_w is then given by

$$\tau_w = -\frac{h}{2}\frac{\mathrm{d}p}{\mathrm{d}x}, \tag{2.2}$$

which implies that the wall shear stress in channel flow can be determined by measuring the pressure gradient. The channel shown in figure 2 was constructed to provide a linear pressure gradient over a large distance, so that the flow is fully developed and $(\mathrm{d}p/\mathrm{d}x)$ can be confidently estimated.

2.2. Working principle of hot-film anemometry

Hot-film anemometry is used to measure the velocity and turbulence properties of fluid flows by measuring the heat dissipated due to convection. The hot-film sensor used in our experiments is shown in figure 3. The H-shaped film at the tip of the sensor is a very thin electrical resistor, through which current is passed, generating heat. The heat transfer rate from the film into the fluid varies with flow velocity according to a modified form of King's law (King, 1914; Dantec, 2023).

https://doi.org/10.1017/flo.2025.10027 Published online by Cambridge University Press

$$q_{\text{conv}} = a + bu^n, \tag{2.3}$$

where a, b, n are constants, and u is the characteristic velocity near the sensor. The heat generated by electric current is

$$q_{\text{gen}} = \frac{E_{\text{a}}^2}{R_{\text{f}}}, \tag{2.4}$$

where E_{a} is the voltage applied across the film, and R_{f} is the film's electrical resistance. A constant-temperature anemometer (CTA) holds R_{f} constant by using a servo amplifier circuit to control the voltage across a Wheatstone bridge, of which the film forms part of one leg. Monitoring this bridge voltage yields E_{a} when the rest of the bridge resistances are known. At constant temperature, energy conservation yields $q_{\text{conv}} = q_{\text{gen}}$. Equations (2.3) and (2.4) can be combined and manipulated to yield the well-known relation

$$E_{\text{a}}^2 = A + B\tau_{\text{w}}^n, \tag{2.5}$$

where τ_{w} is the wall shear stress (Tropea *et al.* 2007). The calibration coefficients A, B, n are determined by correlating the voltage output of the sensor with a known wall shear stress in fully developed channel flow. Because the heat transfer in laminar flow is significantly different than that found in turbulent flow, two sets of coefficients are required for flow fields which contain both regimes.

3. Calibration of hot-film sensor

3.1. Design of channel

The channel used for calibration of the hot-film sensor is motivated by prior work reported in the literature (Sun *et al.* 2018). A schematic of the channel is shown in figure 2(*a*) and a sectional view through a pressure port is shown in figure 2(*c*). The channel was fabricated using aluminium and its cross-section ($w = 50$ mm, $h = 5$ mm) was chosen to target a Reynolds number of $Re = 10{,}000$[1] with the available pump.

The length of the channel was chosen to be $L = 1{,}200$ mm to ensure that the flow would be fully developed over a significant distance. The top of the channel is covered with a clear polycarbonate sheet and leakage is prevented through the use of a gasket along the length of the channel. An aluminium plate is placed over the polycarbonate sheet and clamps are used to apply uniform pressure on the gasket along the length of the channel to make it leak proof – see figures 2(*c*) and 4(*a*).

A submersible utility pump was used to circulate water through the channel. The flow rate is controlled with a gate valve installed upstream of the channel's inlet. The flow is conditioned at the inlet of the channel with a series of baffles, followed by a honeycomb, and then a series of three meshes of decreasing hole size – see figures 2(*b*) and 4(*b*). To reduce the developing length, the boundary layer is tripped with a coarse-grit sand paper strip at the inlet of the channel. The outlet of the channel is connected to a flow conditioner with four internal vanes to minimise end effects – see figure 2(*d*).

To measure pressure along the channel, eight pressure taps are placed on the side of the channel along its length. The ports are 150 mm apart and drilled with a size of 0.8 mm. The ports are connected by a three-way valve – see figure 4(*a*), to a DP15 differential pressure transducer (a product of Validyne Engineering (Validyne 2023), not shown. The pressure differential between ports ② through ⑧ relative to ① are recorded at steady state; the data are then used to compute the pressure at all the ports by assigning an arbitrary pressure to port ⑧ – see figure 5. We observe a linear pressure gradient over the entire measurement section, which indicates that the flow is fully developed downstream of port ①. We mounted the hot-film sensor between ports ④ and ⑤ on the polycarbonate sheet, as shown in figure 4(*a*). A closeup view of the sensor mount is provided in figure 4(*d*). A sectional view of the assembled channel set-up through the sensor mount and sensor is shown in figure 4(*e*). In addition to

[1]The *Re* number is defined based on the bulk velocity, and hydraulic diameter of the channel is used for the characteristic length.

https://doi.org/10.1017/flo.2025.10027 Published online by Cambridge University Press

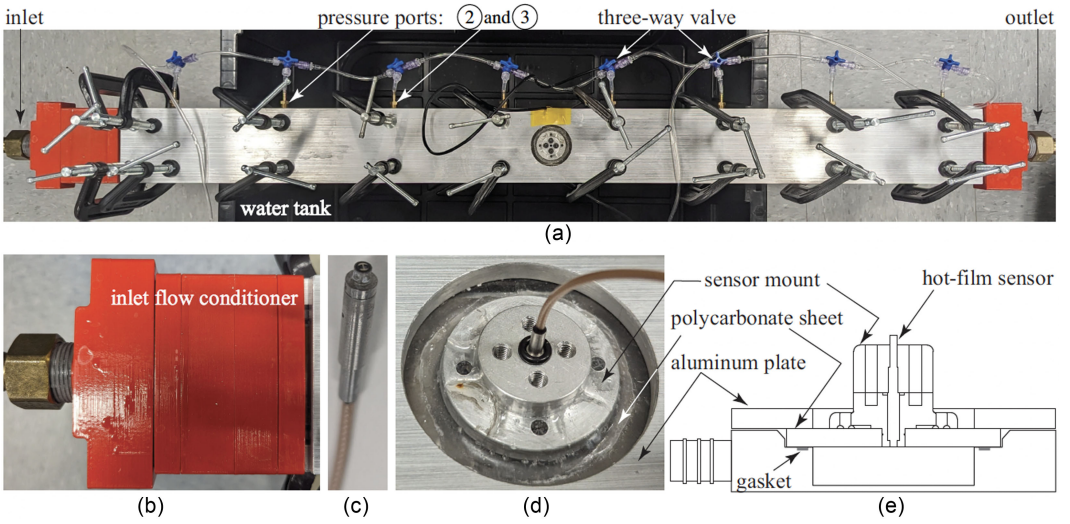

Figure 4. *Assembled view of the channel set-up in figure 2: (a) top view of the channel showing sensor mount (without sensor) and eight pressure ports (see figure 2) connected via three-way valves, (b) inlet flow conditioner, (c) hot-film sensor, (d) magnified view of sensor mount with sensor, (e) sectional view of channel set-up through the sensor mount and sensor.*

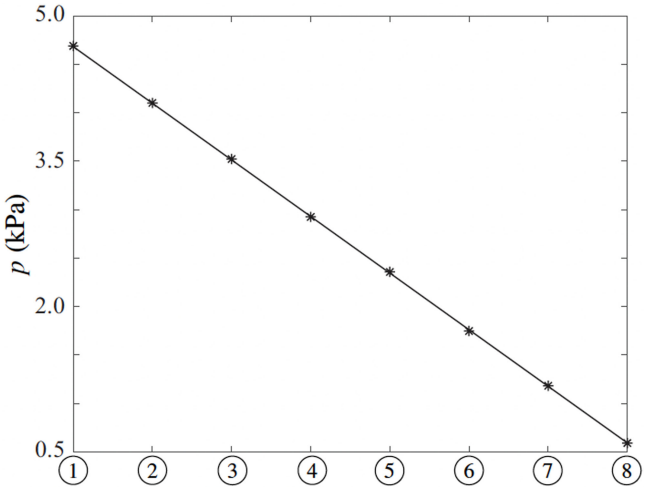

Figure 5. *Pressure at the eight different ports of the channel (see figure 2) for the mass flow rate of 0.422 kg s^{-1}, computed based on pressure differential measurements relative to port ① and assignment of an arbitrary pressure to port ⑧. Note that the straight line fit was obtained by using the data from ports ④ though ⑧.*

making it easier to place our sensor, this mount also provides the same conductive environment between the probe and the wall in both the calibration and the experiment.

3.2. Calibration procedure

The hot-film sensor 55R46, shown in figures 3 and 4(*c*), was calibrated using the constant-temperature anemometer MiniCTA 54T42, also a product of Dantec Dynamics (Dantec 2023). The calibration was

https://doi.org/10.1017/flo.2025.10027 Published online by Cambridge University Press

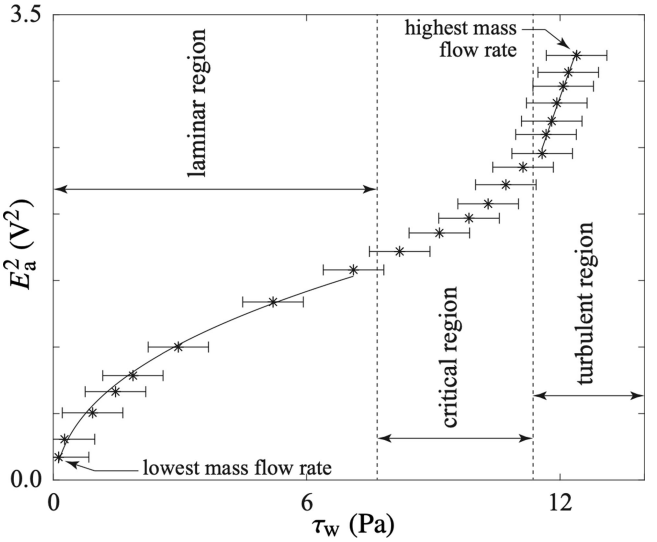

Figure 6. *Calibration data showing the variation of E_a^2 with τ_w. The fitted curves are the same as those shown in figure 7. The error bars indicate the propagation of pressure transducer error (0.5 % of full range) through (2.2). That sensor's full range is 8.6 kPa.*

performed using 21 different flow rates through the channel; a gate valve was installed between the prime mover and the inlet of the channel to control the flow rate. For each flow rate, the pressure transducer and hot-film sensor measurements (voltages) were recorded. The pressure measurement (voltage) provides the pressure drop between ports ④ and ⑤; transducer calibration data are used to express it in Pa and the wall shear stress τ_w is then computed using (2.2). The variation of the square of the hot-film sensor voltage (E_a^2) with the wall shear stress τ_w is plotted in figure 6 with the objective of computing the calibration coefficients in (2.5). It can be seen that the wall shear stress increases monotonically with increase in the mass flow rate.

The variation of E_a^2 with τ_w depicts three distinct behaviours corresponding to three distinct flow regimes: turbulent, critical and laminar. The decision to use separate calibrations for the laminar and turbulent regimes, while not the most common approach in the literature, is scientifically justified based on documented thermal regime-dependent effects. Although Reichert and Azad (1977) and Haselbach and Nitsche (1996) demonstrate that a 1/3 power law between heat transfer and wall shear stress theoretically holds for both laminar and turbulent flows, these studies show that while both regimes follow the same functional form, the fitting coefficients in this relationship are not identical between regimes.

Specifically, Haselbach and Nitsche (1996) note that 'significant differences between the two temperature fields of the test cases occur mainly on the flow side' and demonstrate that laminar flows exhibit 'much more distinct temperature wake' compared with turbulent flows with their 'smaller temperature wake due to increased turbulent heat transport'. These thermal environment differences directly affect the calibration coefficients in the 1/3 power law relationship. This is further supported by Haselbach *et al.* (1995), who provide experimental visualisation showing that 'the surface temperature wake is much greater in the laminar flow compared with the turbulent flow' and emphasise that improved calibration methods should 'take into account the convective as well as the conductive heat loss of a surface hot-film sensor'.

While universal calibrations represent an engineering compromise that uses averaged coefficients across both regimes and works adequately for many applications, the literature evidence suggests this approach prioritises practicality over precision. Even in studies demonstrating universal calibrations, observable scatter and systematic differences between laminar and turbulent data points indicate that

https://doi.org/10.1017/flo.2025.10027 Published online by Cambridge University Press

Table 1. *Calibration coefficients and exponent for laminar and turbulent flow regimes*

Flow regime	A	B	n
Laminar	−0.216	0.798	0.4
Turbulent	−50.86	32.70	0.2

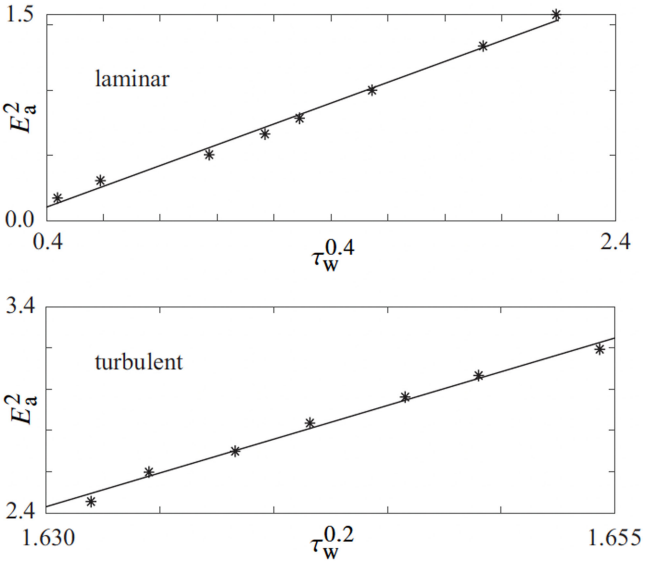

Figure 7. *Linear calibration curves for laminar and turbulent regimes.*

regime-dependent coefficient variations exist but are typically considered acceptable rather than negligible. For applications requiring maximum accuracy, particularly in transitional flows where both regimes may be present, separate calibrations with regime-specific coefficients account for the documented thermal differences and provide superior measurement precision.

The data points corresponding to the laminar and turbulent regimes are used to find a linear fit between E_a^2 and τ_w^n, where the value of the exponent n should lie in the range $[0.1, 0.5]$ – see Tropea *et al.* (2007). A linear fit is found by choosing $n = 0.4$ for the data in the laminar regime and $n = 0.2$ for the data in the turbulent regime. The fitted curves are provided in figures 6 and 7 and the calibration coefficients in (2.5) are provided in Table 1; these coefficients were obtained with an R^2 value of 0.99 and a confidence level of 95 %.

This calibration channel achieved a maximum pressure difference of 4.95 kPa between adjacent ports with the pump running at maximum capacity, resulting in a maximum shear stress of 12.29 Pa. The range of the calibration channel restricts our results to a single operating point (mass flow rate) because of the large variation in shear stress under the Bernoulli pad.

4. Bernoulli-pad experimental set-up

An experimental set-up was developed to measure the wall shear stress generated by a Bernoulli pad. An important component of the set-up is the Bernoulli-pad assembly, comprising the stem, pad and flow conditioning section – see figure 8(*a*,*b*). The stem is a tube with an inside diameter of $d = 25.4$ mm (1.0 in.), an outside diameter of 31.75 mm (1.25 in.) and a length of 88.9 mm (3.5 in.). The pad is a circular, flat plate with a diameter of $D = 203.2$ mm (8.0 in.) and a thickness of 6.35 mm (0.25 in.); this thickness is an important dimension only insofar as it prevents the pad from deflecting under

https://doi.org/10.1017/flo.2025.10027 Published online by Cambridge University Press

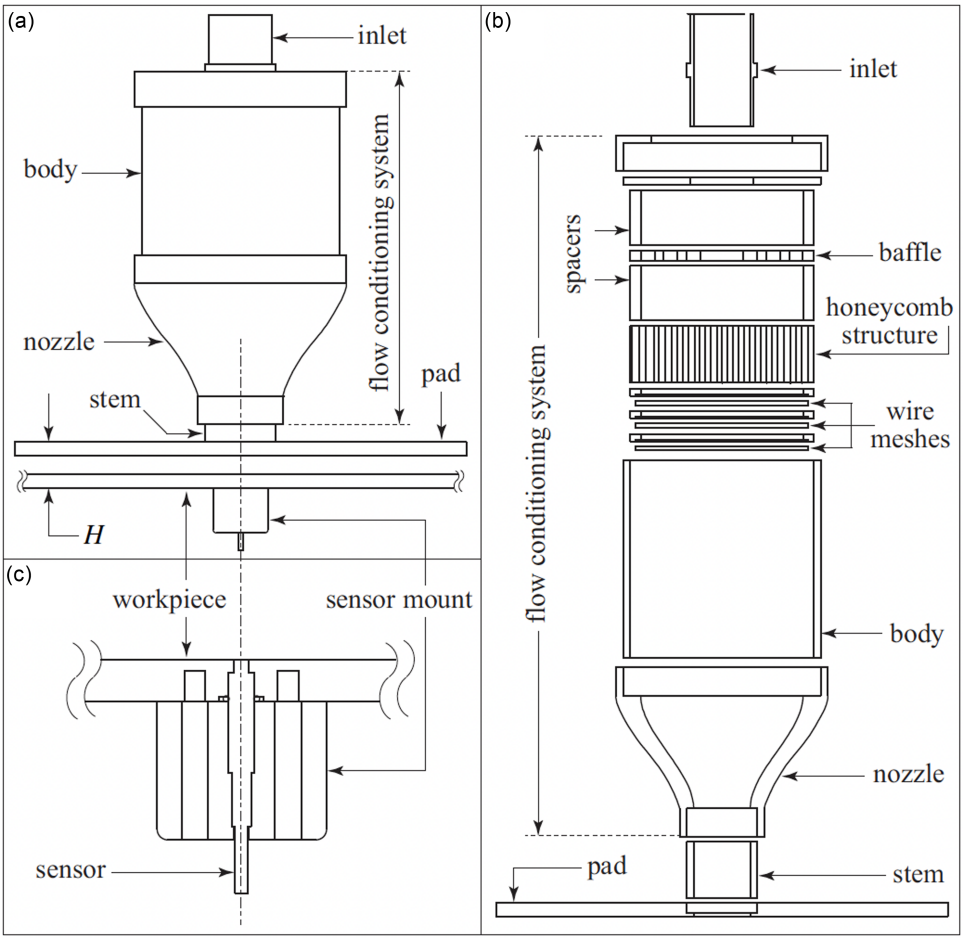

Figure 8. *(a) Bernoulli-pad assembly shown in its nominal configuration over the workpiece, (b) exploded view of Bernoulli-pad assembly, (c) sectional view of flush-mounted sensor in workpiece.*

fluid loads. A 25.4 mm (1.0 in.) hole is located at the centre of the pad along with a 31.75 mm (1.25 in.) counterbore to 75 % depth in the pad. The stem interfaces with the pad in the counterbore such that there are negligible steps for the fluid to encounter. Both the stem and the pad are made of cast acrylic, which has sufficient rigidity and low mean surface roughness depth $0.62\,\mu\text{m} < \text{Rz} < 0.89\,\mu\text{m}$ (Stähli, 2013).

The flow conditioning section is used to obtain a top-hat velocity profile with low turbulence intensity at the inlet of the stem. From upstream to downstream, it is composed of the inlet from the pump, a baffle that breaks down the incoming pipe flow, a honeycomb, three wire meshes of decreasing hole size and a flow contraction – see figure 8(*b*). A cubic equation was used to design the flow contraction profile (Hussain & Ramjee, 1976). The components of the flow conditioning section were mated with the stem in a similar fashion as the stem–pad interface to avoid disturbances in the flow. Except for the inlet, baffle, honeycomb and wire meshes, the materials of the components of the flow conditioning section were chosen as cast acrylic and polyurethane-coated 3D printed PLA for smooth surface finishes.

The apparatus also comprises the workpiece (or wall), sensor mount, linear stage, Bernoulli-pad assembly mount and frame. An assembled view of these components, which we will refer to as the shear test station (STS), is shown in figure 9. The workpiece is a rectangular flat plate (406.4 × 304.8 × 6.35 mm) of 7075-T6 aluminium. The surface of the workpiece was sanded and polished to reduce

https://doi.org/10.1017/flo.2025.10027 Published online by Cambridge University Press

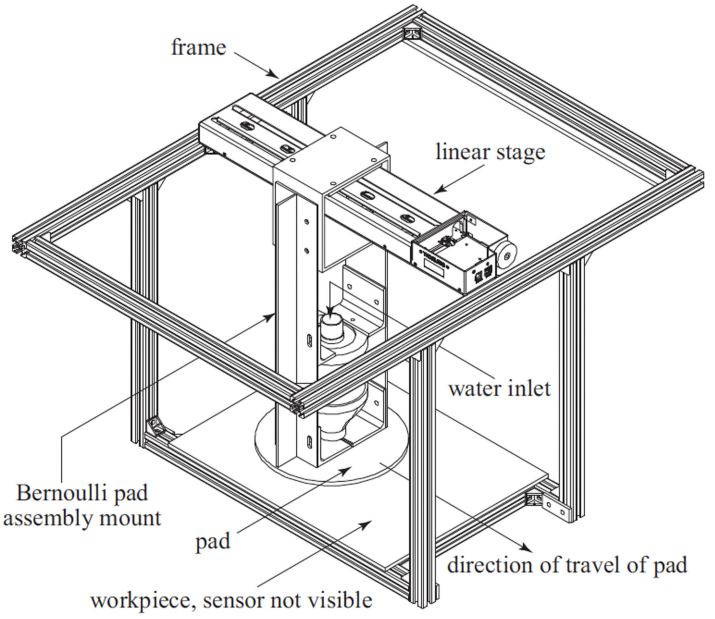

Figure 9. *An assembled view of the shear test station (STS), comprising the Bernoulli-pad assembly mount, workpiece and linear stage.*

its surface roughness. This process typically results in roughness depth levels $0.5\ \mu\text{m} < \text{Rz} < 1.4\ \mu\text{m}$. The sensor mount is placed in a counterbored hole near the centre of the plate which places the sensing surface of the hot-film sensor flush with the workpiece – see figure 8(*c*). The sensor's grounding lead was permanently fastened to one of the plate's vertical faces. Blind holes allow the sensor mount to be secured to the underside of the workpiece.

A LTS300 linear translation stage manufactured by THORLABS (2023) was used to move the Bernoulli pad over the length of the workpiece such that the hot-film sensor can measure the wall shear stress along the radial direction. The stage has an absolute accuracy of 50 μm and a repeatability of 2 μm. The Bernoulli-pad assembly mount, shown in figure 9, is a series of structural aluminium members that interface the Bernoulli-pad assembly in figure 8(*a*) to the linear stage. The joints of the Bernoulli-pad assembly mount are comprise slots and threaded fasteners that allow for setting a uniform gap between the pad and the workpiece and ensure that the pad and the workpiece remain parallel with travel of the linear stage. The fluid power assembly consists of a 250 W submersible pump, rubber hoses and a gate valve for flow rate control.

5. Wall shear stress measurement

5.1. Procedure

The STS was placed into a water tank with dimensions of $2120 \times 749 \times 762$ mm. The frame suspended the workpiece in the centre of the tank's footprint and 356 mm from the bottom. The dimensions of the tank and the location of the workpiece were chosen to ensure that the radial outflow between the pad and workpiece was not affected by the water splashing from the tank walls. Shims were placed between the frame and tank to level the STS before it was secured to the tank with clamps. The pump draws water from beneath the workpiece, and this water is at the ambient temperature (17.25° C) before data collection. The density and viscosity of water at this temperature are $\rho = 998.87\ \text{kg m}^{-3}$ and $\mu = 0.001073\ \text{Pa s}$.

In this experiment, the gap height between the pad and the workpiece was chosen to be $H = 1.3$ mm – see figure 8 (*a*). Shims were placed in the gap to ensure that the gap height was uniform; they were

https://doi.org/10.1017/flo.2025.10027 Published online by Cambridge University Press

removed after ensuring uniform desired gap height. The working mass flow rate was $\dot{m} = 0.046$ kg s^{-1}. This operating point, defined by a combination of H and $\dot{m}$, was chosen to ensure that the maximum shear stress experienced by the hot-film sensor was within our achievable calibration range.[2] At lower flow rates, the relative error at large r increases significantly, along with a tendency of the flow to become visibly non-axisymmetric.

Once the mass flow rate from the pump was at steady state, the linear stage was used to move the Bernoulli pad from its nominal position, and hot-film voltages are measured at each position. At large radii of the Bernoulli pad, we used steps of 5 mm, which is approximately twice the diameter of the hot-film sensor. The step size was reduced to 1.0–2.0 mm close to the neck of the Bernoulli pad, where large variations in the shear stress are expected. The total distance of travel was approximately $\ell = 83.0$ mm, which ensured that the sensor was never exposed to air.

The voltage outputs from the hot-film sensor were first corrected for temperature difference between calibration and wall shear stress measurement conditions using (Bruun, 1995)

$$E_{\text{corr}} = \left(\frac{T_{\text{f}} - T_0}{T_{\text{f}} - T_{\text{a}}}\right)^{0.5} E_{\text{a}},$$

where E_{corr} is the corrected voltage, $T_0 = 25.49°\text{C}$ is the water temperature during calibration, $T_{\text{f}} = 40°\text{C}$ is the film temperature and $T_{\text{a}} = 17.25°\text{C}$ is the water temperature during data acquisition. This film temperature represents an overheat ratio of 0.1. The temperature difference between calibration and experiment is larger than we would have preferred, but this variable was difficult to control between our set-ups. The corrected voltage values were used to obtain the wall shear stress values using (2.5) with the calibration coefficients provided in Table 1.

5.2. Experimental results and comparison with simulation

Numerical simulations were carried out using the Spalart–Allmaras model based on its suitability for adverse pressure gradients (ANSYS, 2022) and the transition-shear stress transport (SST) model due to its extensive use in our prior work with Bernoulli pads (Kamensky *et al.* 2019, 2020; Kamensky, 2020). The latter work and the work in Tomar *et al.* (2022) present PTV data which validate the computational approach used in those works and the present paper over a large section of the flow field. The approach used there did not have sufficient resolution near the wall to resolve the velocity gradient accurately, which pushed us toward the present approach for measuring the wall shear stress. These simulations were carried out for identical flow domain and boundary conditions in the experiments – see figure 10. The domain is axially symmetric without variations in the azimuthal directions. Therefore, we used a two-dimensional axisymmetric model to reduce computational time. Assuming incompressible flow, we imposed a mass flow rate of $\dot{m} = 0.046$ kg/s at the inlet, and exit pressure $p = p_{\text{atm}}$ at the pad's outlet. No-slip conditions were imposed on all solid walls. The computational domain is meshed with quadrilateral dominant elements. The conservation equations are solved using Semi-Implicit Method for Pressure Linked Equations (SIMPLE) algorithm and the pressure and momentum terms are discretised using PREssure STaggering Option (PRESTO)! and second-order discretisation, respectively. The convergence is said to be obtained when the residual is less than 1×10^{-6} for all the variables.

In our experimental set-up, we were careful to choose materials and surface finishes which will allow us to describe the pad and workpiece as 'hydraulically smooth'. This condition is met when $Rz/\delta_l < 5$ (Nikuradse, 1950), where δ_l is the thickness of the laminar sublayer. The representative thickness of our laminar sublayer is $\delta_l = 9.9$ μm based on the maximum measured value of τ_{w}. Given that $Rz < 1.4$ μm for polished aluminium and less for cast acrylic, we satisfy the hydraulically smooth descriptor. In the simulation, we fix surface roughness for the pad and workpiece at $\varepsilon_{\text{p}} = \varepsilon_{\text{w}} = 1$ μm.

[2]Higher mass flow rates are also associated with larger maximum local velocities, which produces cavitation near the neck if water is used as the working fluid; this phenomenon is briefly discussed in Kamensky *et al.* (2020).

https://doi.org/10.1017/flo.2025.10027 Published online by Cambridge University Press

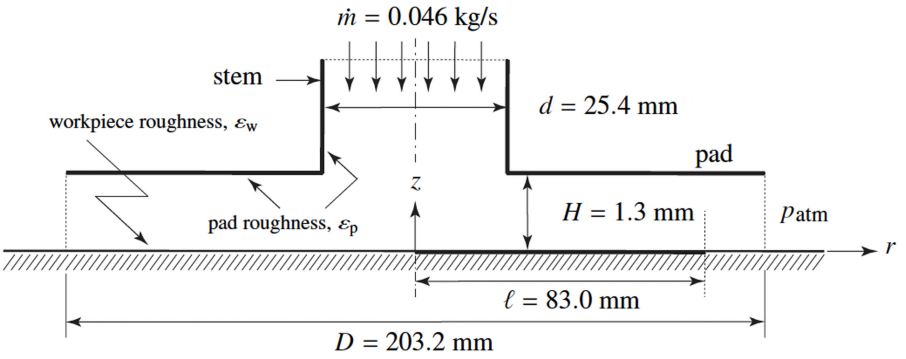

Figure 10. *A schematic of the Bernoulli pad used in simulations.*

In our experiments, the hot-film sensor voltage is obtained for the measurement region of length $\ell = 83.0$ mm shown in figure 10. A comparison of these voltages with the voltage values in figure 7 indicate that the flow is laminar for $0 \le r < 12$ and $14 < r \le 83$ mm and turbulent for $12 \le r \le 14$ mm. The change from laminar to turbulent flow close to the neck of the pad is expected. In this region, the mean velocity is high because of the reduced area relative to the stem. This is amplified by a recirculation region resulting from the sharp corner (Shi & Li, 2016) which further reduces the area through which the flow is moving in the $+r$ direction. The wall shear stress and radial distance are non-dimensionalised using the expressions (Tomar *et al.* 2022)

$$\bar{\tau}_w = \left(\frac{\pi \rho d^3}{4\dot{m}\mu}\right)\tau_w, \qquad \bar{r} = \left(\frac{2}{D}\right). \tag{5.1}$$

The variation in the non-dimensional wall shear stress $\bar{\tau}_w$ with non-dimensional radial distance $\bar{r}$ is shown in figure 11. Contour plots of the radial velocity and pressure are presented in figure 12. There is a separation bubble attached to the corner of the pad at $r = d/2$. This separation bubble reduces the effective cross-sectional area of the flow field under the pad, increasing the local radial velocity and thereby increasing the shear stress on the workpiece – see the inset of figure 11. As the radial flow moves past the separation bubble, there is momentum transferred from the radial direction to the wall-normal direction, yielding a sharp drop in wall shear stress. The momentum recovers its purely radial direction, and since the boundary layer is still very thin, the shear stress increases even though the mean velocity through the cross-section at r is decreasing $\propto r$. However, further downstream, the decreasing mean velocity yields monotonically decreasing wall shear stress. In order to discuss the differences between experiment and simulation, it is helpful to divide the discussion of the data and simulation results into regions of the wall shear stress field.

Before reattachment ($\bar{r} \le 0.14$): there is good agreement between both models and experiment on the values of peak shear. This also suggests that the models are accurately capturing the velocities and extent of the recirculation region. From an application perspective, this is promising; the cleaning efficacy of a Bernoulli pad is characterised by the maximum shear it produces (Kamensky *et al.* 2019), while the deformation and fracture limits on a workpiece are likewise set by the maximum local shear and normal forces. The maximum non-dimensional wall shear stress $\tau_{w,\,max}$ for all cases, including a power law estimation from Tomar *et al.* (2022), is shown in Table 2. In the region where the incoming flow impinges on the wall, the simulations underpredict the experiment. However, this region of the flow is the region which matches the calibration conditions the least well because this is an impingement region, in which the flow is deflected from purely axial to predominantly radial. As opposed to the fully developed boundary layer with zero wall-normal velocity in the calibration channel, this impingement region presents a very strong gradient of wall-normal velocity with a boundary layer that is just starting to develop. In consequence, the correlation between heat dissipation and shear stress would not necessarily follow the same functional form in the impingement region as in the channel.

https://doi.org/10.1017/flo.2025.10027 Published online by Cambridge University Press

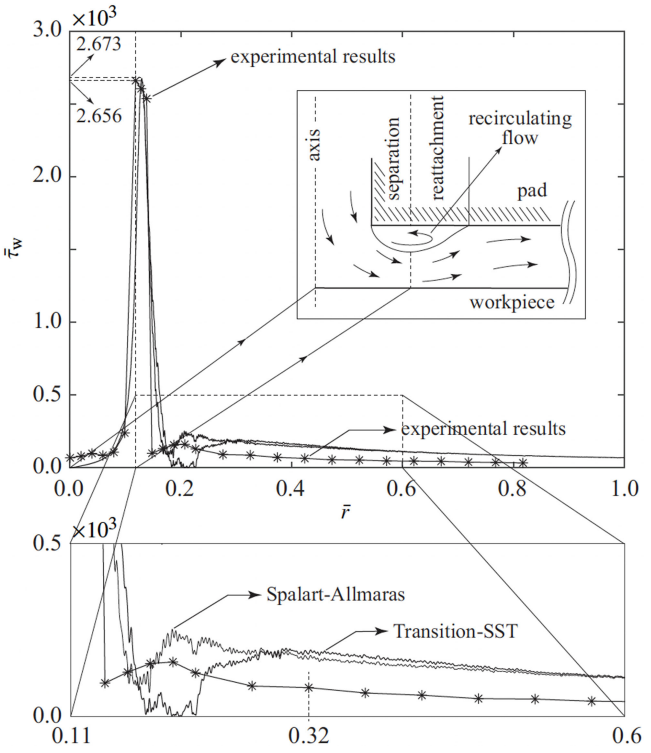

Figure 11. *Variation of $\bar{\tau}_w$ with $\bar{r}$: a comparison of simulation and experimental results. The experimental results, obtained at discrete values of $\bar{r}$, are shown using '$*$' marks. The turbulent calibration coefficients in Table 1 are used from $\bar{r} \in [0.12, 0.14]$, the laminar values are used in the rest of the domain. The top figure shows the recirculation region and the flow around it (Shi & Li, 2016) – see figure inset. A magnified view of the dotted portion of the top figure is shown in the bottom figure for comparison of the two turbulence models with experimental results.*

Fully radial flow ($\bar{r} \geq 0.32$): qualitatively, the gradual decay of wall shear in this region is easily explained by the $1/r$ proportional decay in radial velocity as the cross-sectional area of the gap increases with radius (Guo *et al.* 2017). While the experiments and the simulations both show this behaviour, the models substantially over-predict the experiments. In this region of the flow, the experiment predicts that the flow is laminar. In addition to the two models presented in figure 11, we also ran several other turbulence models with no transition model whatsoever, and these all showed over-prediction of the wall shear stress in this region. The tendency to over-predict was also observed in our prior work (Tomar *et al.* 2022), where a numerical model was compared with PTV data. We tentatively suggest that the over-prediction in this region is driven by a failure to accurately characterise the flow in this region as laminar, and that better predictions at large r will require a model tuned to capture this phenomenon.

Near reattachment ($0.14 < \bar{r} < 0.32$): in this region, there is substantial difference between each model and experiment. All realisations indicate a local minimum followed by a net rise before $r = 0.3$. The experiment shows an immediate rise to a local maximum near $r = 0.2$. The Spalart–Allmaras model was chosen as a candidate model because it was designed to perform well in wall-bounded flows at moderate to low Reynolds numbers under adverse pressure gradients (ANSYS, 2022). The Spalart–Allmaras model indicates a similar local minimum, slightly downstream of experiment. Likewise, the local maximum is further downstream than observed experimentally, consistent with a separation bubble which is larger in the streamwise direction. The four-equation transition-SST model shows a broad region of near-zero shear stress followed by a rise to $r = 0.3$. The $\tau_w \approx 0$ region is likely an indicator

https://doi.org/10.1017/flo.2025.10027 Published online by Cambridge University Press

Table 2. *Dimensionless maximum wall shear stress values obtained from experiment, numerical models and power law (Tomar et al. 2022)*

Experiment	Spalart–Almaras	Transition-SST	Power law
2656.1	2673.1	2676.3	2548.6

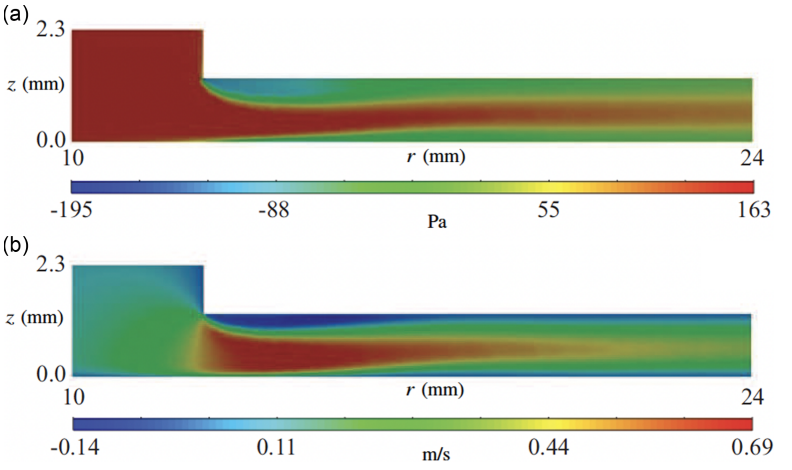

Figure 12. *Contour plots of (a) total pressure and (b) radial velocity in the neck region of the computational domain using the Spalart-Allmaras model.*

of laminar separation (Tomar *et al.* 2022), followed by another transition to turbulence. The cited work found transition SST to perform well in a fully separated flow. However, there are empirical correlations used in the development of the transition-SST model (Menter *et al.* 2006) which were performed on a flat plate. It may be that the current flow field, characterised by sharp radial pressure gradients, presents an out-of-sample challenge for the correlations.

6. Conclusion

The experimental work presented here uses a constant-temperature anemometer with a hot-film sensor to quantify the wall shear stress generated by the action of Bernoulli pad over a proximally located workpiece. An experimental set-up, consisting of a rectangular channel, is designed to calibrate the wall shear stress. The calibration of the sensor is carried out separately for laminar and turbulent regimes. These calibration relations are subsequently used to measure the wall shear stress generated by a Bernoulli pad. It should be mentioned that this experimental effort, which quantifies the wall shear stress generated by a Bernoulli pad with water as the working fluid, is the first of its kind.

The numerical simulations accurately predict the maximum shear stress, and qualitatively correct behaviour, including a secondary peak in the shear stress associated with streamline reattachment and shear stress declining approximately $\propto 1/r$ thereafter. The position of the maximum wall shear stress is found to be very close to the neck of the Bernoulli pad, right below the belly of the recirculation region. The Reynolds-Averaged Navier-Stokes (RANS) computational models we used do not accurately predict the magnitude of the secondary peak, and significantly overpredict the shear stress at large r.

A better turbulence scheme, such as Large Eddy Simulation (LES) or Direct Numerical Simulation (DNS), may provide a better match for the entire domain of $\bar{r}$; however, this will require significantly higher computational effort and lies in the scope of future research. Because the most important aspect of the shear produced by a Bernoulli pad for grooming and cleaning applications is its maximum value, we

https://doi.org/10.1017/flo.2025.10027 Published online by Cambridge University Press

suggest that simpler and faster computational tools are adequate for this purpose. Modelling improvements to better capture the shear stress behaviour at all r should be focused on relaminarisation and reattachment.

Data availability statement. Raw data are available from the corresponding author.

Funding statement. This work was partially funded by the Office of Naval Research: (a) grant no. N00014-22-1-2143, and (b) grant no. N00014-22-1-2170, through a subcontract provided by the University of Massachusetts, Dartmouth.

Competing interests. The authors declare no conflict of interest.

Ethical standards. The research meets all ethical guidelines, including adherence to the legal requirements of the study country.

References

ANSYS fluent: Theory Guide 2022 R2 (Section 4.2.1. Spalart-Allmaras model) (2022). https://ansyshelp.ansys.com/account/secured?returnurl=/Views/Secured/corp/v222/en/flu_th/flu_th_sec_spal_overview.html.

Bellhouse, B., & Schultz, D. (1966). Determination of mean and dynamic skin friction, separation and transition in low-speed flow with a thin-film heated element. *Journal of Fluid Mechanics*, *24*, 379–400.

Brun, X., & Melkote, S. (2009). Analysis of stresses and breakage of crystalline silicon wafers during handling and transport. *Solar Energy Materials and Solar Cells*, *93*, 1238–1247.

Bruun, H. H. (1995). *Hot-wire anemometry*. Oxford University Press.

Dantec Dynamics Flush-mounted hot-film probe. Retrieved 23, January from 2023, http://www.dantecdynamics.com.

Fernholz, H., Janke, G., Schober, M., Wagner, P., & Warnack, D. (1996). New developments and applications of skin-friction measuring techniques. *Measurement Science and Technology*, *7*, 1396.

Guo, J., Shan, H., Xie, Z., Li, C., Xu, H., & Zhang, J. (2017). Exact solution to Navier–Stokes equation for developed radial flow between parallel disks. *Journal Of Engineering Mechanics*, *143*, 04017026.

Haselbach, F., & Nitsche, W. (1996). Calibration of single-surface hot films and in-line hot-film arrays in laminar or turbulent flows. *Measurement Science and Technology*, *711*, 1682–1682.

Haselbach, F., Swoboda, M., Wald, L., & Nitsche, W. (1995). On heat balance and calibration of single-surface hot-films and hot-film arrays in laminar or turbulent flows. In *Symposium on turbulent shear flows* (pp. 13). Pennsylvania State University, University Park.

Hu, P., Xie, Q., Ma, C., & Zhang, G. (2020). Silicone-based fouling-release coatings for marine antifouling. *Langmuir*, *36*, 2170–2183.

Hunsucker, J. T., Hunsucker, K. Z., Gardner, H., & Swain, G. (2016). Influence of hydrodynamic stress on the frictional drag of biofouling communities. *Biofouling*, *32*(10), 1209–1221.

Hussain, A., & Ramjee, V. (1976). Effects of the axisymmetric contraction shape on incompressible turbulent flow. *Journal Of Fluids Engineering*, *98*, 58–68.

Jiang, F., Lee, G., Tai, Y., & Ho, C. (2000). A flexible micromachine-based shear-stress sensor array and its application to separation-point detection. *Sensors and Actuators A: Physical*, *79*, 194–203.

Kahler, C. J., Scharnowski, S., & Cierpka, C. (2012). On the uncertainty of digital PIV and PTV near walls. *Experiments in Fluids*, *52*, 1641–1656.

Kamensky, K. (2020). *A new paradigm for generating surface-normal forces for hull-cleaning robots*. Michigan State University.

Kamensky, K., Hellum, A., Mukherjee, R., Naik, A., & Moisander, P. (2020). Underwater shear-based grooming of marine biofouling using a non-contact Bernoulli pad device. *Biofouling*, *36*, 951–964.

Kamensky, K., Hellum, A., & Mukherjee, R. (2019). Power scaling of radial outflow: Bernoulli pads in equilibrium. *Journal of Fluids Engineering*, *141*, 101201.

King, L., XII (1914). On the convection of heat from small cylinders in a stream of fluid: Determination of the convection constants of small platinum wires with applications to hot-wire anemometry. *Philosophical Transactions of the Royal Society of London. Series A, Containing Papers of a Mathematical or Physical Character*, *214*, 373–432.

Li, X., Cao, Q., & Yu, X. (2024). Experimental investigation and theoretical modeling on Bernoulli gripper using water for supply power enhancement. *Physics of Fluids*, *36*(2), 027120.

Li, X., & Kagawa, T. (2014). Theoretical and experimental study of factors affecting the suction force of a bernoulli gripper. *Journal of Engineering Mechanics*, *140*, 04014066.

Lyu, X., Dai, H., Shi, K., & Li, X. (2024). Experimental study on radial suction flow and its effect in water vortex unit. *Physics of Fluids*, *36*(6), 067116.

McIlwraith, L., & Christie, A. (2003). Contactless handling of objects. U.S. Patent No. 6601888.

https://doi.org/10.1017/flo.2025.10027 Published online by Cambridge University Press

Menesses, M., Belden, J., Dickenson, N., & Bird, J. (2017). Measuring a critical stress for continuous prevention of marine biofouling accumulation with aeration. *Biofouling*, *33*, 1–9.

Menter, F., Langtry, R., Likki, S., Suzen, Y., Huang, P., & Völker, S. (2006). A correlation-based transition model using local variables – Part I: Model formulation. *Journal of Turbomachinery*, *128*, 413–422.

Misimi, E., Oye, E., Lillienskiold, A., Mathiassen, J., Berg, O., Gjerstad, T., Buljo, J., & Skotheim, O. G. R. I. B. B. O. T. 2016, Robotic 3D vision-guided harvesting of chicken fillets. *Computers and Electronics in Agriculture*, *121*, 84–100.

Mykhailyshyn, R., Duchoň, F., Mykhailyshyn, M., & Majewicz Fey, A. (2022). Three-dimensional printing of cylindrical nozzle elements of Bernoulli gripping devices for industrial robots. *Robotics*, *11*, 140.

Naughton, J., & Sheplak, M. (2002). Modern developments in shear-stress measurement. *Progress in Aerospace Sciences*, *38*, 515–570.

Nikuradse, J. (1950). Laws of Flow in Rough Pipes, National Advisory Commission for Aeronautics (NACA) Technical Memorandum 1292, (English translation of 'Stromungsgesetze in Rauhen Rohren'. *vDI-Forschungsheft*, *361*, 1933.

Owen, F. (1970). Transition experiments on a flat plate at subsonic and supersonic speeds. *AIAA Journal*, *8*, 518–523.

Paivanas, J., & Hassan, J. (1981). Attraction force characteristics engendered by bounded, radially diverging air flow. *IBM Journal Of Research and Development*, *25*, 176–186.

Reichert, J. K., & Azad, R. S. (1977). Wall shear stress measurement with a hot film in a variable temperature flow. *Review of Scientific Instruments*, *483*, 341–345.

Sheplak, M., Cattafesta, L., Nishida, T., & Mcginley, C. (2006). MEMS shear stress sensors: Promise and progress. In *IUTAM symposium on flow control and MEMS* (pp. 67–76).

Shi, K., & Li, X. (2016). Optimization of outer diameter of Bernoulli gripper. *Experimental Thermal and Fluid Science*, *77*, 284–294.

Stähli, A. (2013). *The technique of lapping*. Pieterlen/Biel.

Sun, B., Wang, P., Luo, J., Deng, J., Guo, S., & Ma, B. (2018). A flexible hot-film sensor array for underwater shear stress and transition measurement. *Sensors*, *18*, 3469.

Swoboda, M., Haselbach, F., Wald, L., & Nitsche, W. (1993). On surface hot-film applications in laminar-turbulent flows. In *IEEE international congress on instrumentation in aerospace simulation facilities* (pp. 171–178).

THORLABS LTS300. (2023). 300 mm Linear Translation Stage with Integrated Controller, Stepper Motor. (0). Retrieved 26, January from 2023, http://www.thorlabs.com.

Tomar, A., Hellum, A., Kamensky, K., & Mukherjee, R. (2024). Flow physics of a rotating Bernoulli pad: A numerical study. *Journal Of Fluids Engineering*, *146*, 091301.

Tomar, A., Kamensky, K., Mejia-Alvarez, R., Hellum, A., & Mukherjee, R. (2022). A scaling relationship between power and shear for Bernoulli pads at equilibrium. *Flow*, *2*, E29.

Tropea, C., Yarin, A. L., & Foss, J. F. (2007). *Springer handbook of experimental fluid mechanics*. Springer.

Validyne (2023). VALIDYNE Engineering DP15 Variable Reluctance Pressure Sensor Capable of Range Changes. (0). Retrieved 23, January from 2023, http://www.validyne.com.

Wagner, M., Chen, X., Nayyerloo, M., Wang, W., & Chase, J. (2008). A novel wall climbing robot based on Bernoulli effect. In: *2008 IEEE/ASME international conference on mechatronics and embedded systems and applications, MESA 2008* (pp. 210–215).

Winter, K. (1979). An outline of the techniques available for the measurement of skin friction in turbulent boundary layers. *Progress in Aerospace Sciences*, *18*, 1–57.

Yu, X., Zhao, J., & Li, X. (2022). Optimization of mechanical performance of a Bernoulli gripper based on the force characteristic curve synthesis method. *Industrial Robot: The International Journal Of Robotics Research and Application*, *49*, 1169–1177.

Cite this article: Tomar A.S., Perzanowski S., Mejia-Alvarez R., Mukherjee R., Hellum A. and Kamensky K. (2025). Wall shear stress generated by a Bernoulli pad: experiments and numerical simulations. *Flow*, *5*, E33. https://doi.org/10.1017/flo.2025.10027